Powder Technology 407 (2022) 117634

Contents lists available at ScienceDirect

Powder Technology

journal homepage: www.journals.elsevier.com/powder-technology

Elasto-plastic and adhesive contact: An improved linear model and its application

Wenguang Nan [a,b,*], Wei Pin Goh [b], Mohammad Tarequr Rahman [a]

[a] School of Mechanical and Power Engineering, Nanjing Tech University, Nanjing 211816, China
[b] School of Chemical and Process Engineering, University of Leeds, Leeds LS2 9JT, UK

HIGHLIGHTS

- An improved linear elasto-plastic and adhesive contact model is developed.
- Input parameters are significantly reduced compared to other linear models.
- The stiffness and maximum pull-off force in the model are validated.
- Critical plastic-adhesive sticking velocity is investigated.
- Critical yield contact pressure for jump-in induced yielding is analysed.

GRAPHICAL ABSTRACT

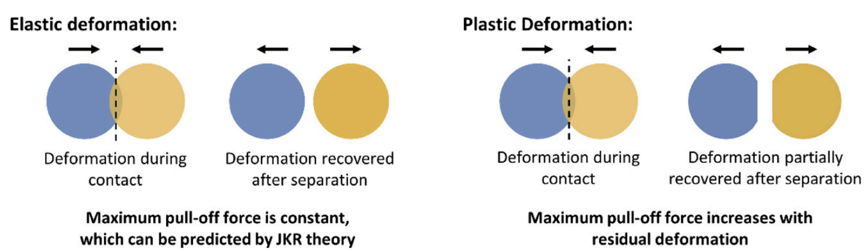

ARTICLE INFO

Keywords:
Contact model
Plastic deformation
Cohesive powder
Sticking velocity
DEM
Flowability

ABSTRACT

An improved linear model is developed for elasto-plastic and adhesive contact. New correlations are proposed and validated to estimate the key parameters of the model, including contact stiffness, yield point, maximum pull-off force and time step. The newly proposed contact model is applied to the analysis of single particle contact behaviour upon impact and bulk particle flow behaviour by DEM simulations. The results show that both single particle and bulk powder behave more “cohesively” if contact plastic deformation is considered. A cohesion yield number is proposed to describe the extent of yielding when cohesive particles are in contact with each other. There is a critical particle size, below which the effect of plastic deformation becomes prominent and must be considered. This provides a new framework and criteria for elasto-plastic and adhesive contact model, and a step towards understanding the effect of plastic deformation on the behaviour of cohesive particles.

1. Introduction

The macroscopic bulk behaviour of powders is governed by the microscopic activities of the individual particles in a granular assembly. Predicting the bulk behaviour of a particulate system requires a thorough understanding of the dynamics of individual particles at microscopic level, but this is very difficult to achieve experimentally. As an alternative method, numerical simulations by Discrete Element Method (DEM) [1] are usually used. In DEM simulation, particle interaction is described by a contact model of choice and particle motion is governed by Newton's law. To accurately represent a realistic particulate system, the particle physical and mechanical properties (e.g. size and shape distribution, Young's modulus, density) and interaction parameters (e.g. friction coefficient, restitution coefficient) should be characterised experimentally at single particle level [2,3], or artificially tuned to produce matching results with the bulk calibration tests (e.g. repose

* Corresponding author at: School of Mechanical and Power Engineering, Nanjing Tech University, Nanjing 211816, China.
E-mail address: nanwg@njtech.edu.cn (W. Nan).

https://doi.org/10.1016/j.powtec.2022.117634
Received 12 April 2022; Received in revised form 4 June 2022; Accepted 12 June 2022
Available online 16 June 2022

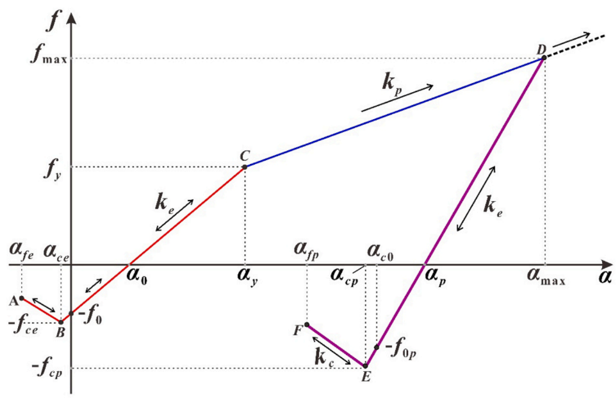

Fig. 1. Schematic diagram of the normal force f-overlap α relationship in the improved linear elasto-plastic and adhesive model.

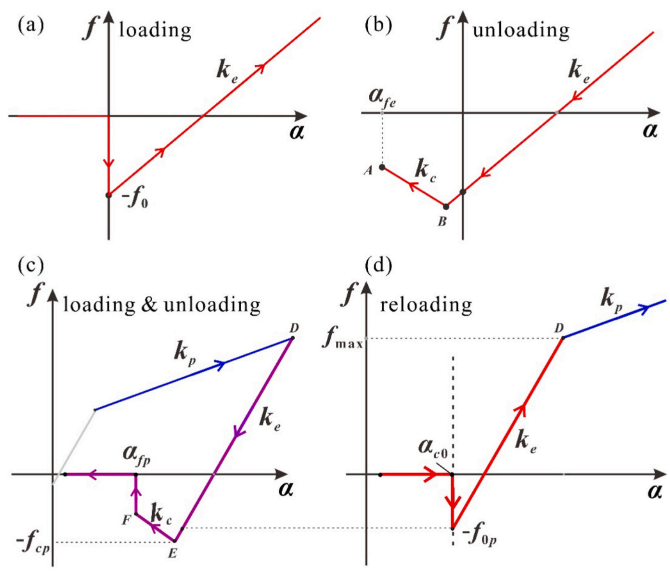

Fig. 2. Schematic diagram of the normal force f-overlap α relationship in the loading/unloading and reloading processes for the contact: (a-b)-without plastic deformation ($f_{\max} < f_y$), where k_e is a constant and corresponds to the lower limit of k_e, and it is assigned as k_{el} for convenience; (c-d)-with plastic deformation ($f_{\max} > f_y$), where k_e varies with $\alpha_{\max}$.

angle, uniaxial compression test) [4], and the contact model should obey realistic physical deformation law of the particle material.

Particle contact can be divided into four classes: elastic, elasto-adhesive, elasto-plastic, and elasto-plastic with adhesion, depending on the material used. For elastic contact, deformation is recoverable, and the normal contact force can be well described by Hertz contact model [5]. For elasto-adhesive contact, as the particles tend to stick to each other, additional energy is required to separate them. The normal contact force in the elasto-adhesive contact can be predicted by JKR theory [6]. JKR theory extends the Hertz model to the elasto-adhesive contact by using an energy balance approach, and the contact area is larger than that of Hertz model. The normal contact force in the elasto-adhesive contact could also be predicted by DMT theory [7], which assumes that the adhesive force does not affect the contact area and considers the adhesive force and Hertz force separately. In DEM simulation, contact is usually assumed to be either elastic or elasto-adhesive, and the aforementioned contact models have been widely applied to simulate various particulate systems, such as coating [8] and powder spreading [2,9]. However, most materials first deform elastically, which then followed by a plastic deformation. This is especially true for rough particles with tiny asperities on the surface. In elasto-plastic contact, a portion of the particle deformation is recoverable, and the rest is permanent. To account for plastic deformation, the normal contact force could be calculated by the non-linear model of Thornton and Ning [10], or the linear model of Walton and Braun [11]. However, in the latter, the initial elastic deformation stage is omitted, which is not realistic. If cohesive force is involved, the contact could become elasto-plastic with adhesion, and the corresponding contact model becomes more complex as the overlap and negative force at the detachment point are affected by plastic deformation (i.e. permanent deformation with flattened area). For this specific type of contact, only a limited number of models are available to estimate the normal contact force of particles for DEM simulation. The latest ones are the non-linear model of Thornton and Ning [10] and the linear models of Pasha et al. [12] and Luding [13]. In the model of Luding [13], the contact breaks at zero overlap, which is unpragmatic since plastic deformation is permanent and hence the detachment must take place at non-zero overlap. This model also assumes that all particles undergo plastic deformation, but in the reality, for dynamic particulate system, the external load applied on the particles at some regions is not large enough to cause yielding and the contact is still elasto-adhesive. In the non-linear model of Thornton and Ning [10], the equations of normal contact force is derived based on material properties and contact mechanics theory, but the governing equations are expressed in a very complex form, and the contact model is very computationally expensive due to its non-linearity nature. The model of Pasha et al. [12] is a linearised version of Thornton and Ning's model [10], and it is more appealing than both the models of Luding [13] and Thornton and Ning [10] in terms of physical nature and computational time. However, Pasha et al. [12] mainly proposed a framework for the contact model, and many details are not provided, such as the unified mathematical equations of the contact force and the criteria for estimation of the contact parameters. Pasha et al. [12] proposed a simplified version for further analysis of the effect of plastic deformation on particle contact behaviour, but the initial elastic process is omitted. It should be noted that in both models of Luding [13] and Pasha et al. [12], the adhesive sticking velocity predicted by JKR theory is not guaranteed anymore.

In this work, an improved linear model is proposed for the elasto-plastic and adhesive contact, and its application for the analysis of the behaviour of single particle contact and bulk particle flow is also focused. A comprehensive description of the mathematical framework of the proposed contact model is firstly given in Section 2. Then the equations to determine key input parameters of this contact model are rigorously derived in Section 3, and these correlations are further validated and compared against the ones digitized from previous literature. In Section 4, the equations to determine the critical sticking velocity are derived, and DEM simulation of single particle contact behaviour upon impact is also carried out, where the proposed contact model is validated against previously experimental data. Then the flowability of bulk powder is analysed in Section 5 to shed light on the combined effects of cohesion and plastic deformation, where the particulate system of FT4 rheometer is simulated. It is followed by the discussions of the advantages of the proposed contact model in Section 6. This work provides a linear elasto-plastic and adhesive contact model, which is well suited for the DEM simulations, and also a step towards understanding the effect of plastic deformation on the sticking velocity of single cohesive particle and flowability of bulk cohesive powder.

2. Description of the proposed contact model

The total contact force, $\boldsymbol{F}$, is the sum of normal contact force $\boldsymbol{f}_n$, tangential contact force $\boldsymbol{f}_t$, and the damping force ($\boldsymbol{f}_{nd}$, $\boldsymbol{f}_{td}$):

$$\boldsymbol{F}_n = \boldsymbol{f}_n + \boldsymbol{f}_{nd} \tag{1}$$

$$\boldsymbol{F}_t = \boldsymbol{f}_t + \boldsymbol{f}_{td} \tag{2}$$

2.1. Normal contact force

The normal contact force $\boldsymbol{f}_n$ is given as:

$$\boldsymbol{f}_n = f\boldsymbol{n} \tag{3}$$

where $\boldsymbol{n}$ is the unit vector in the normal direction; f is the magnitude of normal contact force, which is linear to the normal overlap α, as shown in Fig. 1.

If the maximum load applied is less than the yield force f_y of the particle, there will be no plastic deformation at the end of loading process, thus, the contact behaves elastically with adhesion. In this case, Fig. 1 could be simplified to Fig. 2(a)-(b), where the contact is considered as a linear version of JKR model [5]. During the loading stage, the normal contact force f drops to -f_0 as soon as a contact is established, f then increases linearly with the normal overlap α, the slope of which is dictated by the elastic stiffness k_e. During the unloading stage, the contact force is non-zero even for negative overlap, as further work is required to separate the adhesive contact. The contact breaks at a negative overlap α_{fe} with contact force of -5f_{ce}/9, which is the same as JKR model.

If the maximum load is larger than the yield force f_y, there will be a plastically-deformed domain within the contact area, resulting in plastic deformation before the end of the loading process. At the loading stage, as shown in Fig. 2(c), f increases linearly with the normal overlap, the slope of which follows that of plastic stiffness k_p in the plastic phase, where k_p is usually less than k_e. At the unloading stage, with a decrease in normal overlap, f initially decreases linearly with the elastic stiffness k_e until it reaches point E ($\alpha = \alpha_{cp}, f = -f_{cp}$), where a maximum pull–off force f_{cp} is obtained. f then increases slowly with a stiffness of k_c until it reaches point F ($\alpha = \alpha_{fp}, f = -5f_{cp}/9$), where the particles are detached. If a normal overlap is still identified after the detachment, i.e. the particle centre distance is less than the sum of contact radius, the plastic deformation is maintained. Thus, during the reloading stage, the contact could only be re-established at $\alpha = \alpha_{c0}$ with an initial value of -f_{0p} (i.e. -8f_{cp}/9), as shown in Fig. 2(d). With an increase in normal overlap at the reloading stage, the contact initially behaves elasto-adhesively with a stiffness of k_e until f reaches point D ($\alpha = \alpha_{\max}$), where the maximum normal force in previous loading stage is reached, and then plastic deformation prevails with a plastic stiffness of k_p. It should be noted that $\alpha_{\max}$ is the maximum overlap at which the unloading commences, and it would be only immediately updated and equal to the normal overlap when the contact is yielded again, to prepare for the possible unloading process in the next time step.

For the contact before yielding (i.e. line BC), k_e is a constant and does not vary with normal overlap. However, after the yielding of the contact, k_e would increase with $\alpha_{\max}$, the details of which will be discussed in Section 3.3. Thus, the elastic stiffness k_e of line BC in Fig. 1 corresponds to the lower limit of k_e, and it is assigned as k_{el} for convenience.

Similar to JKR model, f_0 at $\alpha = 0$ in Fig. 1 is given as:

$$f_0 = \frac{8}{9} f_{ce} \tag{4}$$

$$f_{ce} = 1.5\pi\Gamma R^* \tag{5}$$

where f_{ce} is the maximum pull-off force before yielding; Γ is the surface energy; R^* is the equivalent radius. The critical normal overlaps in Fig. 1 are given as:

$$\alpha_0 = \frac{f_0}{k_{el}} = \frac{8}{9}\frac{f_{ce}}{k_{el}} \tag{6}$$

$$\alpha_y = \alpha_0 + \frac{f_y}{k_{el}} \tag{7}$$

$$\alpha_{ce} = \alpha_0 - \frac{f_{ce}}{k_{el}} \tag{8}$$

$$\alpha_{fe} = \alpha_0 - \frac{f_{ce}}{k_{el}} - \frac{4}{9}\frac{f_{ce}}{k_{cl}} \tag{9}$$

$$\alpha_{\max} = \alpha_y + \frac{f_{\max} - f_y}{k_p} \text{ with } \alpha_{\max} = max(\alpha_{\max}, \alpha_y) \tag{10}$$

$$\alpha_p = \left(1 - \frac{k_p}{k_e}\right)(\alpha_{\max} - \alpha_y) + \left(1 - \frac{k_{el}}{k_e}\right)(\alpha_y - \alpha_0) + \alpha_0 \tag{11}$$

$$\alpha_{c0} = \alpha_p - \frac{8}{9}\frac{f_{cp}}{k_e} \tag{12}$$

$$\alpha_{cp} = \alpha_p - \frac{f_{cp}}{k_e} \tag{13}$$

$$\alpha_{fp} = \alpha_p - \frac{f_{cp}}{k_e} - \frac{4}{9}\frac{f_{cp}}{k_c} \tag{14}$$

where α_p is derived from the normal force at point D:

$$k_p(\alpha_{\max} - \alpha_y) + f_y = k_e(\alpha_{\max} - \alpha_p) \tag{15}$$

$$\alpha_p = \left(1 - \frac{k_p}{k_e}\right)\alpha_{\max} + \frac{k_p\alpha_y - f_y}{k_e} \tag{16}$$

For the contact before yielding, $\alpha_{\max}$ in Eq. (10) is mathematically reduced to $\alpha_{\max} = \alpha_y$ while k_e is reduced to its minimum value (i.e. k_{el}), thus, Eq. (11) is reduced to $\alpha_p = \alpha_0$, and f_{cp} is reduced to $f_{cp} = f_{ce}$ (shown in Section 3.4), k_c is reduced to k_{cl} (shown in Section 3.2), resulting in $\alpha_{fp} = \alpha_{fe}$, $\alpha_{cp} = \alpha_{ce}$, and $\alpha_{c0} = 0$. Therefore, Eqs. (11–14) could be deemed as a general mathematical form for the calculation of critical normal overlaps, which are valid for both the contacts before and after yielding.

The non-zero normal force could be classified into three states, f_c for line AB or EF, f_e for line BC or DE, f_p for line CD:

$$f_e = k_e(\alpha - \alpha_p) \tag{17}$$

$$f_p = f_y + k_p(\alpha - \alpha_y) \tag{18}$$

$$f_c = -f_{cp} + k_c(\alpha_{cp} - \alpha) \tag{19}$$

Thus, the normal force f in Fig. 1 is mathematically given as:

$$f = \begin{cases} f_e & \alpha > \alpha_{cp} \& f_p > f_e \\ f_p & \alpha > \alpha_{cp} \& f_p \le f_e \\ f_c & \alpha_{fp} \le \alpha \le \alpha_{cp} \\ 0 & \alpha < \alpha_{fp} \ \| \ cs = 0 \end{cases} \tag{20}$$

where "$cs = 0$" refers to the states: first loading with $\alpha < 0$ (Fig. 2(a)) and reloading with $\alpha < \alpha_{c0}$ (Fig. 2(d)). It should be noted that Eqs. (17)–(20) are valid for both the contacts before and after yielding. For example, for the contact before yielding, as shown above, $k_e = k_{el}$, $\alpha_p = \alpha_0$, thus, Eq. (17) is simplified to $f_e = k_{el}(\alpha - \alpha_0)$, which is intuitively expected in Fig. 1.

2.2. Tangential contact force

The tangential contact force $\boldsymbol{f}_t$ is given as:

$$\boldsymbol{f}_t = k_t\boldsymbol{\delta}_t \tag{21}$$

where $\boldsymbol{\delta}_t$ is the vector of tangential displacement; k_t is tangential stiffness, which can be related to k_n [5]:

$$\frac{k_t}{k_n} = 4\frac{G^*}{E^*} \tag{22}$$

where G^* and E^* are the equivalent shear modulus and Young's

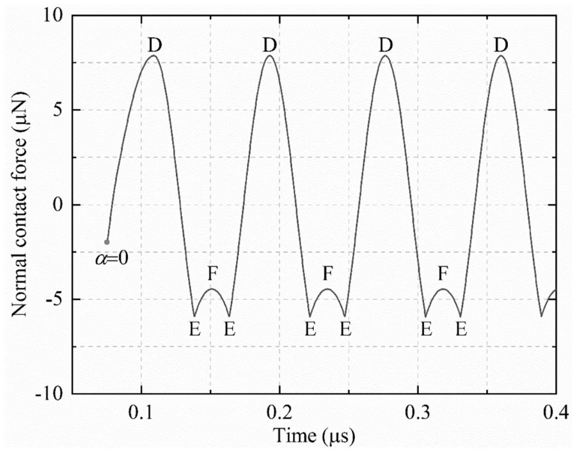

Fig. 3. Example of the oscillation of normal contact force with time if there is no viscous damping after yielding.

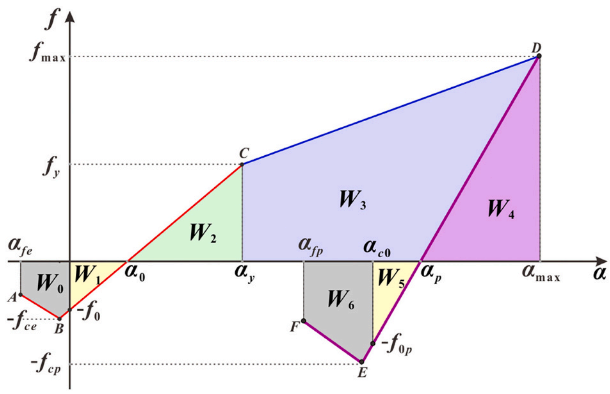

Fig. 4. Work of deformation due to normal contact force in different contact stages.

modulus, respectively; k_n is the normal stiffness, i.e. k_c for line AB or EF, k_e for line BC or DE, k_p for line CD, as shown in Fig. 1. For the sliding contact, i.e. $k_t|\boldsymbol{\delta}_t| > \mu f$, the energy is dissipated from the interfacial sliding without introducing the viscous damping in the tangential direction. Thus, Eq. (2) is reduced to $\boldsymbol{F}_t = \boldsymbol{f}_t$, given as:

$$\boldsymbol{F}_t = \mu f \frac{\boldsymbol{\delta}_t}{|\boldsymbol{\delta}_t|} \tag{23}$$

where μ is the sliding friction coefficient; f is normal force in Eq. (20).

2.3. Damping force

For the contact before yielding, besides the frictional dissipation through interfacial sliding and adhesive work, the energy dissipation is mainly attributed to the viscous elastic damping, especially in the normal direction. The damping force in the normal and tangential direction is given as:

$$f_{nd} = 2\gamma\sqrt{m^* k_n}\boldsymbol{V}_n \tag{24}$$

$$f_{td} = 2\gamma\sqrt{m^* k_t}\boldsymbol{V}_t \tag{25}$$

where γ is the damping coefficient due to viscous and viscoelastic damping effect or energy dissipation of elastic wave propagation; m^* is the equivalent mass; $\boldsymbol{V}_n$ and $\boldsymbol{V}_t$ are the relative velocity in normal and tangential direction, respectively. γ is related to elastic restitution coefficient e_0, given as:

$$\gamma = -\beta \frac{\ln e_0}{\sqrt{\pi^2 + (\ln e_0)^2}} \tag{26}$$

where $\beta = 1$ is the damping factor.

For the contact after yielding, the energy dissipation of elastic wave propagation during impact is very small, compared to the ones due to plastic deformation, as reported by Ning et al. [14], indicating that viscous elastic damping could be ignored (i.e. $\beta = 0$). However, in the impact test, if the viscous damping force is omitted while the particle could not rebound, the contact force oscillates indefinitely along line D-E-F (Fig. 1), and a state of equilibrium can never be achieved as no energy is dissipated, as shown in Fig. 3. Meanwhile, the material is not perfectly plastic. Therefore, a small value of β (e.g. 0.1) is necessary, although its contribution to total energy dissipation can be ignored.

3. Key parameters of the contact model

In the improved contact model, the key parameters, i.e. yield point (f_y, α_y), stiffness (k_e, k_c, k_p) and maximum pull-off force (f_{cp}), are related to the work of deformation shown in Fig. 4, and they are discussed in this section. The physical nature of the contact is well kept during the derivation as shown below, and the proposed correlations are validated against the data digitized from the literature.

3.1. Contact force and normal overlap at yield point, f_y and α_y

The contact force and normal overlap at the yield point (point C in Fig. 1) are evaluated by assuming the same yield work as predicted by Thornton and Ning [10], given as:

$$W_2 = \frac{f_y^2}{2k_{el}} = W_y = \frac{(\pi R^* p_y)^5}{60E^{*4}R^{*2}} \tag{27}$$

Thus, the yield force and the corresponding normal overlap are given as:

$$f_y = f_{y0}\sqrt{\frac{6}{5}\frac{k_{el}}{\pi R^* p_y}} \tag{28}$$

$$\alpha_y - \alpha_0 = \frac{f_y}{k_{el}} = \alpha_{y0}\sqrt{\frac{8}{15}\frac{\pi R^* p_y}{k_{el}}} \tag{29}$$

where f_{y0} and α_{y0} are the yield force and the corresponding normal overlap predicted by Thornton and Ning [10] in their non-linear contact model:

$$f_{y0} = \frac{\pi^3 R^{*2} p_y^3}{6E^{*2}} \tag{30}$$

$$\alpha_{y0} = \frac{\pi^2 R^* p_y^2}{4E^{*2}} \tag{31}$$

where p_y is the limiting contact pressure of the softer particle, i.e. $p_y = \min(p_{y1}, p_{y2})$. p_y is related to the yield stress σ_y, given by Jackson & Green [15]:

$$p_y = C\sigma_y \tag{32}$$

where C is a coefficient related to its Poisson's coefficient ν, given by $C = 1.295\exp(0.736\nu)$. It is similar to the model given by Chang et al. [16]:

$$p_y = KH \tag{33}$$

where K is the hardness factor, given by $K = 0.454 + 0.41\nu$; and H is the hardness, given by $H = 2.8\sigma_y$. In particulate systems, i.e. $\nu = 0.2$– 0.4, both models give almost the same ratio of the yield contact pressure to yield stress, $p_y/\sigma_y = 1.4$– 1.7, as shown in Fig. 5.

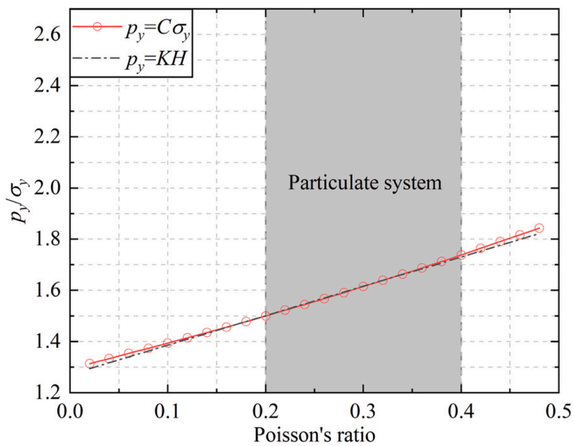

Fig. 5. Variation of the ratio of yield contact pressure p_y to yield stress σ_y with Poisson's ratio.

For most particulate systems, the yield stress can be evaluated from the quasi-static test, i.e. nano-indentation test, the data of which can be referred to the material database or handbook. However, for the particulate systems with high collision velocity, such as impact breakage, the yield stress is dynamic and sensitive to the strain rate [14,17]. In this case, the yield stress should be experimentally evaluated from the dynamic test (e.g. dropping hammer experiment), which could be fitted by the following model:

$$\sigma_y = \sigma_y^{\ s}\left(1 + Yln(V_i/V_0)\right) \tag{34}$$

where V_i is the characteristic strain rate of the particulate system in the simulation; σ_y is the characteristic yield stress at V_i; σ_y^s is quasi-static yield stress measured at the specified strain state V_0; Y is an empirical parameter determined experimentally by the dynamic test.

3.2. Stiffness k_c

As shown in Fig. 2(b), for the contact without yielding, the adhesive sticking work W_0 needs to be overcome to separate the particles in contact. W_0 is assumed to be the same as traditional JKR model, given as:

$$W_0 = \frac{56}{162}\frac{f_{ce}^{\ 2}}{k_{cl}} + \frac{17}{162}\frac{f_{ce}^{\ 2}}{k_{el}} = W_{JKR} \tag{35}$$

where the derivation of W_0 is shown in Appendix A; k_{el} and k_{cl} are the stiffnesses of the contact before yielding, corresponding to the lower limit of k_e and k_c, respectively. The ratio of k_{cl} to k_{el} is given as:

$$\frac{k_{cl}}{k_{el}} = \frac{\frac{56}{162}\frac{f_{ce}^{\ 2}}{k_{el}}}{W_{JKR} - \frac{17}{162}\frac{f_{ce}^{\ 2}}{k_{el}}} \tag{36}$$

where W_{JKR} is given as [5]:

$$W_{JKR} = 7.09\left(\frac{\Gamma^5 R^{*4}}{E^{*2}}\right)^{1/3} \tag{37}$$

Substituting Eqs. (5) and (37) into Eq. (36), given as:

$$\frac{k_{el}}{k_{cl}} = 0.92\frac{k_{el}}{\Gamma^{1/3}E^{*2/3}R^{*2/3}} - 0.3 \tag{38}$$

For the particle properties used in this work, k_{el}/k_{cl} predicted by Eq. (38) is larger than 1. If comparing k_{cl} to the normal stiffness at $\alpha = 0$ predicted by Hertz model with JKR theory, it is given as:

$$\frac{k_{el}}{k_{cl}} = 1.13\frac{k_{el}}{k_{H-JKR,\alpha=0}} - 0.3 \tag{39}$$

$$k_{H-JKR,\alpha=0} = 1.23\left(\Gamma E^{*2} R^{*2}\right)^{1/3} \tag{40}$$

where the derivation of $k_{H\text{-}JKR,\ \alpha=0}$ is shown in Appendix B. Thus, the stiffness k_{cl} in Eq. (38) is very close to the stiffness at $\alpha = 0$ predicted by Hertz model with JKR theory.

For the contact after yielding (Fig. 2(c)-(d)), although k_e in the unloading process increases with the maximum load, the ratio of k_e/k_c is assumed to be the same as k_{el}/k_{cl} predicted by Eq. (38).

3.3. Stiffness k_e

In the unloading process after yielding, i.e. line DE in Fig. 1, the elastic stiffness k_e should vary with $\alpha_{\max}$, as reported by Luding [13], Pasha et al. [12], Thornton et al. [18]. In the work of Luding [13] and Pasha et al. [12], k_e varies linearly with $\alpha_{\max}$. However, as reviewed by Thornton et al. [18], k_e should be a linear function of $\sqrt{\alpha_{\max}}$. This is also in accordance with Hertz model:

$$k_H = \frac{df_H}{d\alpha} = 2E^* R^* \sqrt{\alpha/R^*} \tag{41}$$

where $f_H = 4/3E^*R^{*1/2}\alpha^{3/2}$ is the elastic force in Hertz model. Here, considering its physical nature, in the linear elasto-plastic and adhesive contact model developed in this work, k_e is defined as:

$$k_e = k_{em}\sqrt{\frac{\alpha_{\max}}{R^*}} \tag{42}$$

where k_{em} is assumed to be the maximum stiffness at a normal overlap of R^*.

The elastic stiffness k_e in Eq. (42) can be evaluated through the given unloading line after yielding, i.e. k_{e0} at $\alpha_{\max 0}$ is known, given as:

$$k_{em} = k_{e0}\sqrt{\frac{R^*}{\alpha_{max0}}} \tag{43}$$

Thus, k_e for line DE is given as:

$$k_e = k_{e0}\sqrt{\frac{\alpha_{\max}}{\alpha_{max0}}} \tag{44}$$

For the contact before yielding, i.e. $\alpha < \alpha_y$ for line BC, k_{el} is the lower limit of k_e, and it is calculated by substituting $\alpha_{\max} = \alpha_y$ into Eq. (44), given as:

$$k_{el} = k_e\left(\alpha_{\max} = \alpha_y\right) = k_{e0}\sqrt{\frac{\alpha_y}{\alpha_{max0}}} \tag{45}$$

As α_y is a function of k_{el}, as shown in Eq. (29), Eq. (45) should be solved together with Eq. (29) in an iterative fashion by initially assuming $\alpha_y = \alpha_{y0}$.

The elastic stiffness k_e in Eq. (42) can also be evaluated through the stiffness of the contact before yielding, i.e. k_{el} for line BC in Fig. 1 is known. In this case, α_y can be directly calculated from Eq. (29). Similar to Eq. (44), the elastic stiffness k_e for line DE is given as:

$$k_e = k_{el}\sqrt{\frac{\alpha_{\max}}{\alpha_y}} \tag{46}$$

In the work of Luding [13] and Pasha et al. [12], to avoid k_e being less than k_p at small plastic deformation, k_p is included into the calculation of k_e. If applying this concept to Eq. (42), k_e is then given as:

$$k_e = k_p + \left(k_{em} - k_p\right)\sqrt{\frac{\alpha_{\max}}{R^*}} \tag{47}$$

$$k_e = k_p + \left(k_{e0} - k_p\right)\sqrt{\frac{\alpha_{\max}}{\alpha_{max0}}} \tag{48}$$

Table 1
Particle properties used in the work of Ning (1995) and Du et al. (2007).

Properties	Ning	Du et al.
Radius (μm), R	2.45	4
Density (kg/m^3), ρ	1350	–
Young's modulus (GPa), E	1.2	410
Poisson's ratio, ν	0.3	0.3
Surface energy (J/m^2), Γ	0.2	1.0
Yield pressure (MPa), p_y	35.3	5.52×10^3 *
$\pi R^* p_y$ (N/m)	272	6.94×10^4

* Calculated from the yield stress ($p_y = C\sigma_y$).

Table 2
Re-calculated particle contact parameters based on the plot in Ning (1995) and Du et al. (2007).

Parameters	Ning	Du et al.
	42.4	8584.4
f_{max} (μN)	20.9	5170.7
	8.3	2132.2
	210.5	53.7
α_{max} (nm)	112.6	35.7
	53.9	17.9
	177.3	33.4
α_p (nm)	91.1	20.2
	41.3	8.2
	8.4	321.5
f_{cp} (μN)	6.1	239.7
	4.6	170.8
	1274	4.2×10^5
k_e (N/m)	958	3.3×10^5
	639	2.2×10^5
k_p (N/m)	217	1.8×10^5

$$k_{el} = k_p + \left(k_{e0} - k_p\right)\sqrt{\frac{\alpha_y}{\alpha_{max0}}} \tag{49}$$

To validate these two methods (i.e. without and with involving k_p during the calculation of k_e), the force-overlap response of loading/unloading predicted by Ning [14] and Du et al. [19] is used. In the work of Ning [14], the impact test of an ammonium fluorescein particle to a silicon target at three impact velocity (i.e. 2, 5 and 10 m/s) is analysed by using the non-linear elasto-plastic and adhesive model developed by Thornton and Ning [10], while in the work of Du et al. [19], the indentation test of a ruthenium particle to a rigid and flat surface is analysed by using finite element model. The particle properties used in their work are shown in Table 1, and the equivalent Young's modulus is given by $E^* = E/(1\text{-}\nu^2)$ as the wall in their work has a much larger Young's modulus than that of the particle. By using the Digitizer Tool of Origin software (Originlab, USA), f_{max}, α_{max}, α_p and f_{cp} are digitized from the three unloading curves in their work, as shown in Table 2, and k_e and k_p are re-calculated as:

$$k_{e,i} = \frac{f_{max,i}}{\alpha_{max,i} - \alpha_{p,i}} \qquad (i = 1-3) \tag{50}$$

$$k_p = \frac{1}{2}\left(\frac{f_{max,1} - f_{max,2}}{\alpha_{max,1} - \alpha_{max,2}} + \frac{f_{max,2} - f_{max,3}}{\alpha_{max,2} - \alpha_{max,3}}\right) \tag{51}$$

By specifying the maximum value of α_{max} and the corresponding elastic stiffness k_e in Table 2 as α_{max0} and k_{e0}, respectively, the variation of k_e with normal overlap can be predicted by Eq. (44) or Eq. (48), as shown in Fig. 6. The prediction of Hertz model is also included in Fig. 6, which is the same as that of JKR theory at the same normal overlap for the unloading process with plastic deformation (i.e. $\alpha >> \alpha_0$), as shown in Appendix B.

In Fig. 6(a), the prediction of Eqs. (42)–(45) agrees well with the ones re-calculated from Ning et al. [14], which is intuitively expected as both of them are originated from Hertz model. According to the theory of Thornton [5], k_e should be less than the value predicted by Hertz model (i.e. Eq. (41)) if cohesion and plastic deformation have significant effects on the unloading process. As shown in Fig. 6(a), k_e predicted by Eqs. (42)–(45) fulfils this criterion even at small plastic deformation. On the contrary, k_e is overestimated by Eqs. (47–49) especially at small plastic deformation, as k_p contributes more to k_e than that of $\alpha_{max}^{0.5}$ at small α_{max}. In fact, in Eqs. (42–45), the minimum predicted value of k_e is always larger than k_p, as long as the contact in the unloading process obeys the same law of Hertz theory. Thus, k_p is not needed in the calculation of k_e as they are actually independent parameters from the physics point of view.

In Fig. 6(b), the prediction of Eqs. (42–45) agrees better with the ones re-calculated from Du et al. [19] than that of Eqs. (47)–(49). The elastic stiffness in Du et al. [19] is very large, resulting in small effects of adhesion and plastic deformation on the unloading process. Thus, k_e is very close to the ones predicted by Hertz model, which is very different to the work of Ning [14]. It should be noted that in the finite element simulation of Du et al. [19], different assumptions are used and k_p decreases significantly at small plastic deformation. Thus, if using Eqs. (47–49) to calculate k_e, a smaller and changeable k_p should be used for the comparison with k_e at small plastic deformation.

The contact parameters at the yield point (i.e. $\alpha = \alpha_y$) is shown in Table 3. In the theory of Thornton and Ning [10], the plastic loading line is tangential to the elastic loading curve predicted by Hertz model, resulting in k_e at the yield point being equal to $\pi R^* p_y$ while $k_p = k_e$. In this work, k_{el} predicted by Eq. (45) is very close to $\pi R^* p_y$, which agrees

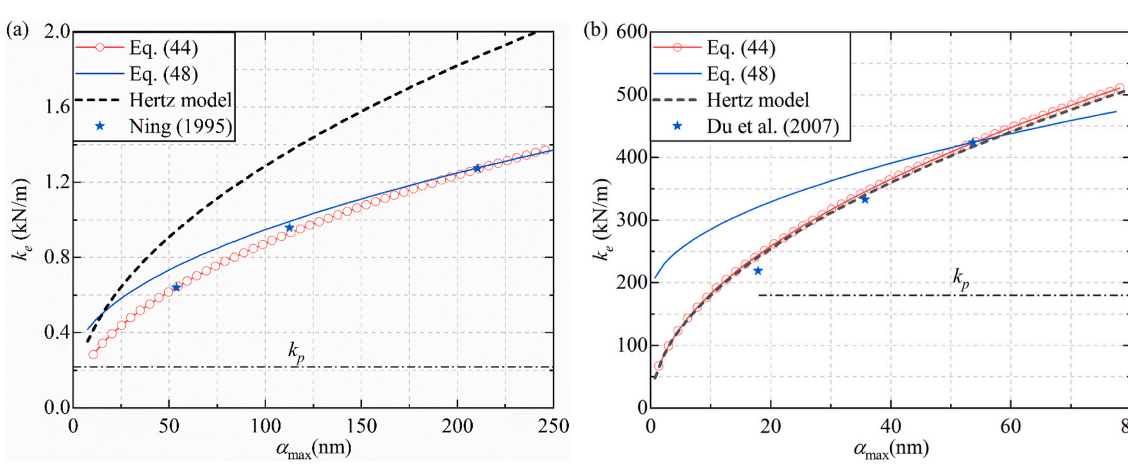

Fig. 6. Comparisons of stiffness k_e predicted by different methods with (a) Ning (1995) and (b) Du et al. (2007) under different maximum normal overlaps α_{max} (i.e. the overlap at which the unloading commences).

Table 3
Particle contact parameters at the yield point ($\alpha = \alpha_y$) for the particles used in Ning (1995) and Du et al. (2007).

	Parameters	$k_e = k_{e0}\sqrt{\frac{\alpha_{max}}{\alpha_{max0}}}$	$k_e = k_p + (k_{e0} - k_p)\sqrt{\frac{\alpha_{max}}{\alpha_{max0}}}$
Ning	k_{el}, N/m	283	418
	k_H ($\alpha = \alpha_y$), N/m	416	353
	α_y, nm	10.4	7.5
	α_0, nm	7.3	4.9
	k_{el}/k_{cl}	1.8	2.7
Du et al.	k_{el}, N/m	6.7×10^4	2.1×10^5
	α_y, nm	1.35	0.71
	α_0, nm	0.25	0.08
	k_{el}/k_{cl}	3.9	12.6

well with this theory, whilst k_{el} predicted by Eq. (49) is much overestimated. Thus, k_e in the following sections is calculated by Eqs. (42–45) unless otherwise specified. Meanwhile, if there are no experimental data available for the input parameters, i.e. k_p, and k_{el} (or α_{max0} and k_{e0}), the following value is recommended for k_{el}, and k_p could be assumed to be the same as k_{el}.

$$k_{el} = 2E^*\sqrt{R^*\alpha_{y0}} = \pi R^* p_y \tag{52}$$

3.4. Maximum pull-off force f_{cp}

Compared to the contact before yielding, more adhesive sticking work is needed to separate the adhesive particles with plastic deformation. The increment is due to the flattening of the contact area, given as:

$$W_6 - W_0 = \pi {a_{res}}^2 \Gamma \tag{53}$$

where a_{res} is the contact area at the residual deformation α_{res}, and $a_{res}^2 = R^*\alpha_{res}$ is assumed. To be consistent with the reloading process shown in Fig. 2(d), where the contact could re-establish at the normal overlap α_{c0}, the residual deformation is assumed to be $\alpha_{res} = \alpha_{c0}$. Thus, α_{res} could be reduced to 0 for the contact without plastic deformation, which is intuitively expected. According to Eqs. (5–6, 12), the right-hand side of Eq. (53) is given as:

$$\pi {a_{res}}^2\Gamma = \pi\Gamma R^*\alpha_{c0} = \pi\Gamma R^*\left(\alpha_p - \frac{8}{9}\frac{f_{cp}}{k_e}\right) = \frac{2}{3}\left(f_{ce}\alpha_p - f_{cp}\alpha_0\frac{k_{el}}{k_e}\right) \tag{54}$$

According to Eqs. (A1) and (A6), the left-hand side of Eq. (53) is given as:

$$\begin{aligned} W_6 - W_0 &= \frac{16}{27}\frac{1}{A}\left(\frac{{f_{cp}}^2}{k_e} - \frac{{f_{ce}}^2}{k_{el}}\right) = \frac{16}{27}\frac{f_{ce}}{A}\frac{f_{ce}}{k_{el}}\left(\frac{{f_{cp}}^2}{{f_{ce}}^2}\frac{k_{el}}{k_e} - 1\right) \\ &= \frac{2}{3}\frac{f_{ce}\alpha_0}{A}\left(\frac{{f_{cp}}^2}{{f_{ce}}^2}\frac{k_{el}}{k_e} - 1\right) \end{aligned} \tag{55}$$

where A is given as:

$$A = \frac{16}{27}\Big/\left(\frac{56}{162}\frac{k_{el}}{k_{cl}} + \frac{17}{162}\right) = \frac{16}{27}\Big/\left(\frac{56}{162}\frac{k_e}{k_c} + \frac{17}{162}\right) \tag{56}$$

Substituting Eqs. (54, 55) into (53) yields:

$$\frac{k_{el}}{k_e}\frac{{f_{cp}}^2}{{f_{ce}}^2} - 1 = A\left(\frac{\alpha_p}{\alpha_0} - \frac{k_{el}}{k_e}\frac{f_{cp}}{f_{ce}}\right) \tag{57}$$

which can be further simplified as:

$$\left(\frac{f_{cp}}{f_{ce}}\right)^2 + A\frac{f_{cp}}{f_{ce}} - \left(\frac{\alpha_p}{\alpha_0}A + 1\right)\frac{k_e}{k_{el}} = 0 \tag{58}$$

Thus, the maximum pull-off force f_{cp} is given as:

$$\frac{f_{cp}}{f_{ce}} = \frac{-A + \sqrt{A^2 + 4\frac{k_e}{k_{el}}\left(\frac{\alpha_p}{\alpha_0}A + 1\right)}}{2} \tag{59}$$

For the contact before yielding, i.e. $\alpha_p = \alpha_0$, $k_e = k_{el}$, Eq. (59) is mathematically simplified to $f_{cp} = f_{ce}$. Thus, Eq. (59) is a general form for both contacts before and after yielding shown in Fig. 2.

In the work of Pasha et al. [12], f_{cp} is given as:

$$f_{cp} = -\sqrt{\frac{162}{137}\pi\Gamma R^* k_e(\alpha_p - \alpha_y)\left(2 - \frac{\alpha_p - \alpha_y}{R^*}\right)} \tag{60}$$

which is derived for constant k_e. If considering the fact that k_e varies with α_{max}, it can be further simplified by using similar derivations as above, given as:

$$\begin{aligned} \frac{f_{cp}}{f_{ce}} &= \sqrt{\frac{162}{137}\frac{\pi\Gamma R^*}{f_{ce}}\frac{k_e}{f_{ce}}(\alpha_p - \alpha_y)\left(2 - \frac{\alpha_p - \alpha_y}{R^*}\right)} \\ &= \sqrt{B\frac{k_e}{k_{el}}\frac{(\alpha_p - \alpha_y)}{\alpha_0}\left(2 - \frac{\alpha_p - \alpha_y}{R^*}\right)} \end{aligned} \tag{61}$$

$$B = \frac{162}{137} \times \frac{16}{27} = \frac{96}{137} \approx 0.7 \tag{62}$$

For the case with small plastic deformation, i.e. α_{max} is slightly larger than α_y but with $\alpha_p < \alpha_y$, Eq. (60) or Eq. (61) will predict zero pull-off force, which is unrealistic.

Thornton and Ning [10] also proposed a method to calculate f_{cp} in their non-linear model, which is given as:

$$\frac{f_{cp}}{f_{ce}} = \frac{R_{eff}}{R^*} \tag{63}$$

where R_{eff} is the effective curvature due to contact flattening, and it is calculated from the equivalent elasto-adhesive normal force f_{eq} at the same contact radius from which unloading commences. If applying this method to the linear model in this work, it is given as:

Table 4
Summary of the calculation methods of maximum pull-off force.

Formulations	Equation number	Remarks
$\frac{f_{cp}}{f_{ce}} = \frac{-A + \sqrt{A^2 + 4\frac{k_e}{k_{el}}\left(\frac{\alpha_p}{\alpha_0}A + 1\right)}}{2}$	(59)	$A = \frac{\frac{16}{27}}{\frac{56}{162}\frac{k_e}{k_c} + \frac{17}{162}}$
$\frac{f_{cp}}{f_{ce}} = \sqrt{0.7\frac{k_e}{k_{el}}\frac{(\alpha_p - \alpha_y)}{\alpha_0}\left(2 - \frac{\alpha_p - \alpha_y}{R^*}\right)}$	(61)	re-derived based on Pasha et al. (2014)
$\frac{f_{cp}}{f_{ce}} = \frac{f_y + k_e(\alpha_{max} - \alpha_y)}{f_y + k_p(\alpha_{max} - \alpha_y)}$	(64)	not suitable for constant k_e (i.e. not varying with α_{max})
$\frac{f_{cp}}{f_{ce}} = \left(\frac{k_e}{k_{el}}\right)^{3/2}$	(67)	not suitable for constant k_e (i.e. not varying with α_{max})

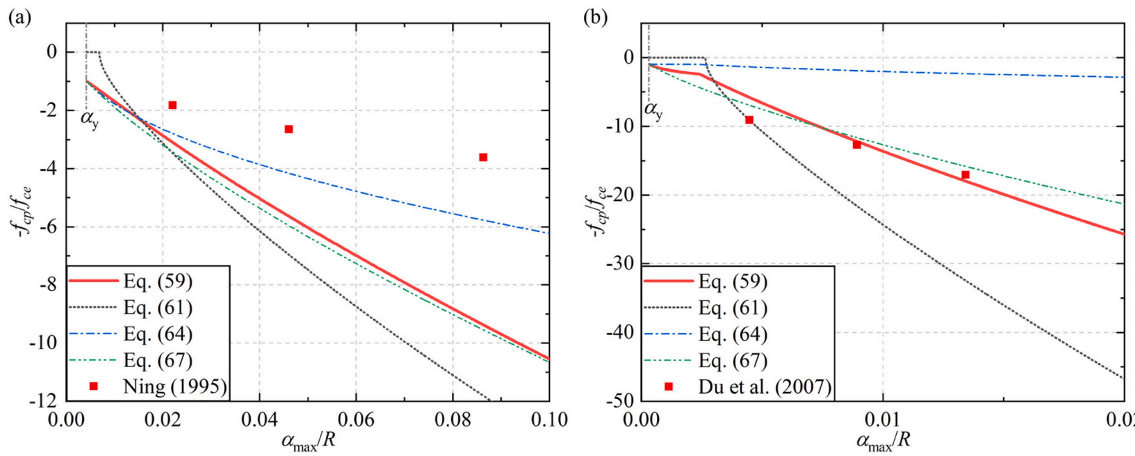

Fig. 7. Comparisons of maximum pull-off force f_{cp} predicted by different methods with (a) Ning (1995) and (b) Du et al. (2007) under different maximum normal overlaps α_{max} (i.e. the overlap at which the unloading commences).

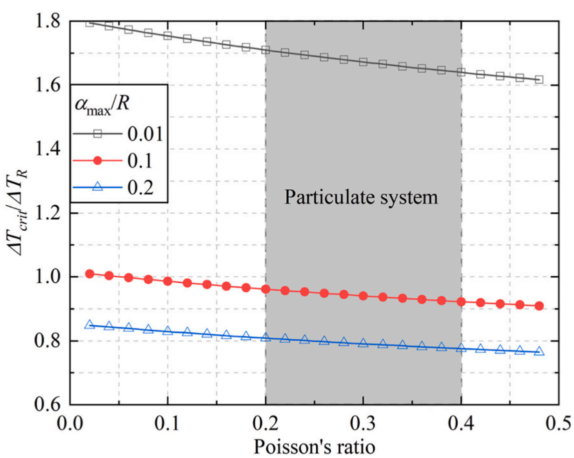

Fig. 8. Variation of the ratio of critical time step ΔT_{crit} to Rayleigh time step ΔT_R with Poisson's ratio.

$$\frac{f_{cp}}{f_{ce}} = \frac{R_{eff}}{R^*} = \frac{f_{eq}}{f_{max}} = \frac{f_y + k_e(\alpha_{max} - \alpha_y)}{f_y + k_p(\alpha_{max} - \alpha_y)} \tag{64}$$

For large loading force (i.e. large α_{max}), f_{cp}/f_{ce} approaches to k_e/k_p.

Eq. (37) can also be used to estimate the adhesive work for the contact with plastic deformation by replacing R^* with R_{eff}, given as:

$$\frac{W_6}{W_0} = \left(\frac{R_{eff}}{R^*}\right)^{4/3} = \left(\frac{f_{cp}}{f_{ce}}\right)^{4/3} \tag{65}$$

According to Appendix A, the ratio of W_6 to W_0 is given as:

$$\frac{W_6}{W_0} = \left(\frac{f_{cp}}{f_{ce}}\right)^2 \left(\frac{k_e}{k_{el}}\right)^{-1} \tag{66}$$

Substituting Eq. (66) into Eq. (65) gives:

$$\frac{f_{cp}}{f_{ce}} = \left(\frac{k_e}{k_{el}}\right)^{3/2} \tag{67}$$

These calculation methods are summarised in Table 4. In the work of Pasha et al. [12], a constant k_e is used to check the sensitivity of f_{cp} to α_p. However, in that case, Eq. (64) predicts a constant f_{cp} at large plastic deformation whilst Eq. (67) gives $f_{cp} = f_{ce}$. Thus, only the case of varying k_e with α_{max} is focused here.

The predictions of these methods are compared with the results in Ning [14] and Du et al. [19], as shown in Fig. 7, with the particle properties and parameters shown in Tables 1–3. Here, k_e is calculated based on Eq. (46) with k_{el} in Table 3. For the ruthenium particle in Du et al. [19], k_p shows a decrease at small plastic deformation but the decrement is not provided in their work, thus, k_p is set to be k_p = minimum(k_p, k_e) for the calculations shown in Fig. 7 for convenience. For ammonium fluorescein particle, all methods predict a larger f_{cp} than that of the non-linear elasto-plastic and adhesive contact model in Ning et al. [14]. For ruthenium particle, compared to the FEM results in Du et al. [19], Eq. (64) largely underestimates the f_{cp}, but Eqs. (59) and (67) show a good agreement, whilst Eq. (61) overestimates f_{cp} significantly. Meanwhile, Eq. (61) predicts f_{cp} to be less than f_{ce} at small plastic deformation, which is not realistic. Thus, the predictions of Eqs. (59) and (67) are more practical than Eqs. (61) and (64).

3.5. Time step

The critical time step can be estimated from the single degree-of-freedom system of a mass m connected to ground by a spring of stiffness k_e, for which the critical time step ΔT_{crit} is given as:

$$\Delta T_{crit} = 2\sqrt{\frac{m}{k_e}} \tag{68}$$

As shown in section 3.3, k_e in the unloading process is less than the ones predicted by Hertz model:

$$k_e \le 2ER\sqrt{\alpha_{max}/R} \tag{69}$$

Thus, the critical time step could be given as:

$$\Delta T_{crit} = \pi R \sqrt{\frac{\rho}{E}} \sqrt{\frac{8}{3\pi}} \left(\frac{\alpha_{max}}{R}\right)^{-1/4} \tag{70}$$

The critical time step based on Rayleigh surface wave is given as [20]:

$$\Delta T_R = \frac{\pi R}{0.1631\upsilon + 0.8766}\sqrt{\frac{\rho}{G}} \tag{71}$$

By comparing Eqs. (70, 71), given as:

$$\frac{\Delta T_{crit}}{\Delta T_R} = \frac{0.1631\upsilon + 0.8766}{\sqrt{1+\upsilon}} \sqrt{\frac{4}{3\pi}} \left(\frac{\alpha_{max}}{R}\right)^{-1/4} \tag{72}$$

The variation of $\Delta T_{crit}/\Delta T_R$ with Poisson's ratio ν is shown in Fig. 8. For most particulate systems, $0.2 \le \nu \le 0.4$, $\Delta T_{crit}/\Delta T_R$ is 0.9–1.0 for $\alpha_{max}/R = 0.1$. As the maximum normal overlap is usually less than $0.1R$ and $\Delta T_{crit}/\Delta T_R$ is inversely proportional to α_{max}/R, $\Delta T_{crit}/\Delta T_R$ could be roughly assumed to be 1 (using its lower limit). Therefore, the time step in DEM simulation for the contact model developed in this work could also be evaluated from the Rayleigh time step in Eq. (71).

It should be noted that the above analysis only provides the maximum limit of the time step, as it does not consider the details of the contact process. Thus, the value of time step used in DEM simulation should be evaluated based on the particulate systems. For most simulation systems, $\Delta t = (0.1\text{–}\ 0.25)\Delta T_R$ can be adopted for a good balance between the computational time and accuracy, which is similar to the cases using Hertz contact model [5]. For particulate systems with high collision velocity, e.g. impact of particle against a wall, to accurately detect the contact details (e.g. the line EF in Fig. 1), much smaller time step is conservatively suggested, e.g. $\Delta t = 0.01\text{–}\ 0.1\Delta T_R$.

3.6. Summary of the evaluation of key parameters

In the contact model developed in this work, several parameters are involved, but most of them can be calculated based on the contact properties of single particle. For example, f_y from Eq. (28), α_y from Eq. (29), k_c from Eq. (38) or Eq. (39), k_e from Eq. (46) for the contact after yielding, f_{cp} from Eq. (59). Thus, apart from the particle properties and interaction parameters in conventional contact models (i.e. Hertz-Mindlin model), such as Young's modulus, friction coefficient, etc., there are only four additional input parameters: surface energy Γ, two stiffnesses (i.e. stiffness k_{el} for the contact before yielding, plastic stiffness k_p), and yield contact pressure p_y. Auto-calculation and estimation of the parameters involved in the model could be found from Excel worksheet in Supplementary Material. These parameters could be easily calculated from various single particle characterisation techniques, as described below. The evaluation of these parameters from the characterisation test of bulk powder (such as Shear Cell and FT4 rheometer) may also be possible in the future.

1) Surface energy Γ: it can be experimentally measured from the drop test [21] or centrifuge method [22]. However, for particle with large surface energy and small yield contact pressure, the experiment test could lead to large error (i.e. the contact is already yield during the test). In this case, surface energy Γ can be roughly estimated from Hamaker constant of material [23] and then further calibrated by DEM simulation of bulk particle flow.
2) Stiffnesses k_{el} and k_p: plastic stiffness k_p is calculated directly from the loading curve, while minimum elastic stiffness k_{el} could be calculated by Eq. (45) with k_{e0} and $\alpha_{\max 0}$ extracted from unloading curve, where large loading force is needed to yield the contact in the indentation test. If no experimental data of the loading/unloading curves is available, k_{el} can be estimated from yield contact pressure using Eq. (52), and k_p can be assumed to be the same as k_{el}.
3) Yield contact pressure p_y: it could be preferentially calculated from the yield stress σ_y using Eq. (32) or Eq. (33). If high impact velocity is involved, the sensitivity of yield stress to strain rate should be considered by Eq. (34). The yield stress here is referred to the compressing yield stress instead of the pulling yield stress. Usually, σ_y/E is 0.001– 0.1 for most materials [17,19,24,25]. As the state of the contact (yield or not) is strongly determined by the yield contact pressure, σ_y should be carefully examined or calibrated.

4. Critical sticking velocity

In this section, the normal impact of a spherical particle against a plane wall is simulated, and the effect of yield contact pressure on the critical sticking velocity is investigated. The proposed contact model is also further validated against the experimental data in the literature. The value of the critical sticking velocity and parameters involved in following derivation could be quickly examined through Excel worksheet in Supplementary Material.

Based on the surface energy Γ and yield contact pressure p_y, three kinds of characteristic velocity could be obtained from Fig. 4 and Appendix A:

$$V_s = \sqrt{\frac{2W_0}{m^*}} = 1.84\frac{(\Gamma/R)^{5/6}}{\rho^{1/2}E^{*1/3}} \tag{73}$$

$$V_{y0} = \sqrt{\frac{2W_2}{m^*}} = \sqrt{\frac{f_y^{\,2}}{m^* k_{el}}} = \left(\frac{\pi}{2E^*}\right)^2\left(\frac{2}{5\rho}\right)^{1/2} p_y^{\,5/2} \tag{74}$$

$$V_y = \sqrt{\frac{2(W_2 - W_1)}{m^*}} = \sqrt{\frac{f_y^{\,2} - f_0^{\,2}}{m^* k_{el}}} \tag{75}$$

where $m = m^*$ is the particle mass; $R = R^*$ is the particle radius; V_s is the adhesive sticking velocity without considering plastic deformation, below which the particle will stick to the wall due to the adhesive work, and V_s here has the same value as predicted by JKR theory; V_{y0} is the yielding velocity without considering cohesion effect, above which the contact will have plastic deformation; V_y is the corresponding yielding velocity when the cohesion effect is included.

If the particle approaches the plane wall, it will gain energy as a result of the attractive force between them (i.e. negative force, $f = -f_0$ to $f = 0$ in line BC in Fig. 1). Thus, the total initial energy involved in the impact is given as:

$$W_i = \frac{1}{2}mV_i^{\,2} + W_1 \tag{76}$$

where the effects of potential energy (i.e. gravity) and viscous damping are omitted. When the particle velocity is reduced to zero, part of total initial energy is converted into stored elastic energy, W_e, and the remainder is dissipated through plastic deformation, (W_i–W_e). If the stored elastic energy, W_e, is larger than the adhesion work W_c required to separate the particle from the wall, then the particle will rebound. Otherwise, the particle will remain adhered to the wall. The plastic adhesive sticking velocity V_{ys} is defined as the critical impact velocity, at which the bound velocity is zero, i.e. $W_e = W_c$. Depending on the yield contact pressure, at the impact velocity of $V_i = V_{ys}$, the contact could be yielded or not yielded at the end of the loading process. The critical yield contact pressure distinguishing these two cases is governed by either of the following criteria:

$$W_0 = W_2 - W_1 \; or \; V_y = V_s \tag{77}$$

For the case with $V_y < V_s$, the contact starts yielding before the end of the loading process at the impact velocity of $V_i = V_{ys}$. In this case, the plastic adhesive sticking velocity V_{ys} is strongly affected by the maximum pull-off force f_{cp}. According to Appendix A, W_e and W_c at the impact velocity of $V_i = V_{ys}$ are given as:

$$W_e = W_4 = \frac{f_{\max}^{\,2}}{2k_e} = W_c = W_5 + W_6 = \frac{1}{2}\frac{f_{cp}^{\,2}}{k_e}\left(1 + \frac{56}{81}\frac{k_e}{k_c}\right) \tag{78}$$

where f_{max} is related to the impact kinetic energy:

$$\frac{mV_{ys}^{\,2}}{2} = -W_1 + W_2 + W_3 + W_4 = \frac{mV_y^{\,2}}{2} + \frac{f_{\max}^{\,2} - f_y^{\,2}}{2k_p} \tag{79}$$

By initially assuming $f_{\max} = f_y$, V_{ys} could be obtained using an iterative method: $\alpha_{\max}$ from Eq. (10), k_e from Eq. (46), f_{cp} from Eq. (59), V_{ys} from Eq. (79), and then new $f_{\max}$ from Eq. (78) for next iteration. For the case with $V_y \geq V_s$, the contact has not yet yielded at the end of the loading process at the impact velocity of $V_i = V_{ys}$, thus, V_{ys} is not affected by f_{cp}, and it is given by $V_{ys} = V_s$.

The variation of plastic adhesive sticking velocity V_{ys} with yield contact pressure p_y is shown in Fig. 9, where viscous damping is not included. The physical properties of the ammonium fluorescein particle and silicon wall are shown in Table 5, which are updated and summarised by Kim and Dunn [26]. The adhesive sticking velocity is $V_s =$ 0.66 m/s. Instead of using the fitting value (k_e, k_p) in Table 2, k_p is assumed to be equal to be k_{el}, and k_{el} is given by Eq. (52). At small yield

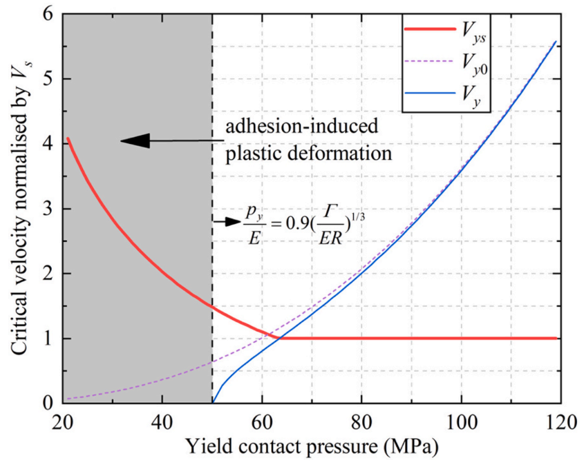

Fig. 9. Variation of critical velocity with yield contact pressure, where the velocity is normalised by adhesive sticking velocity V_s predicted by JKR theory; V_{ys} is the critical sticking velocity considering both cohesion and plastic deformation; V_{y0} (not considering cohesion effect) and V_y (considering cohesion effect) are the yielding velocity, above which the contact could be yielded.

Table 5
Physical properties of particle and wall in the normal impact test.

Properties	Particle	Wall
Radius (μm), R	2.45	–
Density (kg/m^3), ρ	1350	2330
Young's modulus (GPa), E	1.2	166
Poisson's ratio, ν	0.33	0.28
Yield pressure (MPa), p_y	–	120
Surface energy (J/m^2), Γ	0.24	

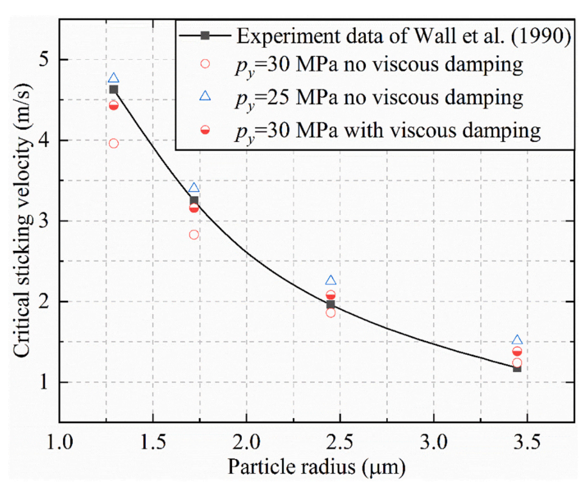

Fig. 10. Comparisons of critical sticking velocity V_{ys} predicted by this work with the experimental data of Wall. et al. (1990).

contact pressure, V_{ys} is much larger than V_s, which is expected for adhesive contact with plastic deformation. With an increase in yield contact pressure, V_{ys} decreases until it reaches the critical point, where p_y meets the criterion of Eq. (77). With a further increase in the yield contact pressure, V_{ys} does not change anymore and remains equal to the adhesive sticking velocity V_s.

It should be noted that there is a special case, i.e. $f_y < f_0$ or $W_2 < W_1$ in Fig. 4, as shown in the shadow zone in Fig. 9, in which the attractive force (such as van der Waals force) would always induce plastic deformation as long as the particles can be brought into contact. This is

Table 6
Critical sticking velocity V_{ys} for different particle size.

Particle properties	Radius (μm)	3.445	2.45	1.72	1.29	Mean relative error
	V_s (m/s)	0.49	0.66	0.88	1.12	
V_{ys}	Wall. et al. (1990)	1.18	1.96	3.25	4.63	–
	$p_y = 25$ MPa, $e_0 = 1$	1.51	2.25	3.4	4.76	12.5%
	$p_y = 30$ MPa, $e_0 = 1$	1.24	1.86	2.83	3.96	9.4%
	$p_y = 30$ MPa, $e_0 = 0.81$	1.38	2.08	3.16	4.43	7.5%

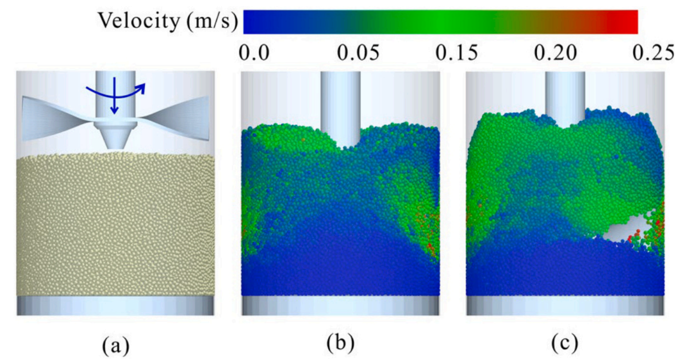

Fig. 11. Snapshots of particle flow (Γ = 27 mJ/m^2) in FT4 rheometer: (a) initial particle bed with blade rotating anti-clockwise while penetrating down; (b) reference case considering only cohesion (using Hertz model with JKR theory); (c) considering both cohesion and plastic deformation (using the linear elasto-plastic and adhesive contact model developed in this work); (b) and (c) are at both the same penetration depth (i.e. time) and viewpoint.

Table 7
Physical properties of particle and geometry in the flowability measurement by FT4 rheometer.

Properties	Particle	Blade	Vessel
Radius (mm), R	0.2–0.3	–	–
Density (kg/m^3), ρ	2500	7800	2500
Young's modulus (MPa), E	63	210	63
Poisson's ratio, ν	0.2	0.3	0.2
Contact yield pressure (MPa), p_y	0.5	–	–

Table 8
Interaction parameters of particle and geometry in the flowability measurement by FT4 rheometer.

Interaction parameters	Particle-Particle	Particle-Blade	Particle-Vessel
Restitution coefficient, e_0	0.93	0.95	0.93
Sliding friction, ρ	0.5	0.3	0.5
Surface energy (mJ/m^2), Γ	3.5, 27	3.1	2.6

known as adhesion-induced plastic deformation or jump-in induced plastic deformation. If k_{el} is given by Eq. (52), the critical yield contact pressure could be derived from $f_y = f_0$ or $W_2 = W_1$, given as:

$$\frac{p_y}{E} = \frac{2}{\pi^{2/3}}\left(\frac{5}{6}\right)^{1/6}\left(\frac{\Gamma}{ER}\right)^{1/3} = 0.9\left(\frac{\Gamma}{ER}\right)^{1/3} \quad (80)$$

Thus, large surface energy corresponds to larger critical yield contact pressure. A non-dimensional number, cohesion-yield number, is proposed here:

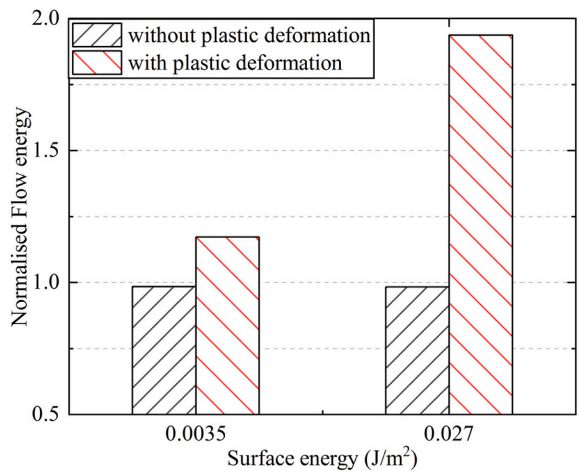

Fig. 12. Flow energy of cohesive powder in FT4 rheometer predicted by the linear elasto-plastic and adhesive contact model: without and with considering plastic deformation; the flow energy is calculated at the penetration depth of 10 mm and normalised by the ones predicted by the DEM simulation using Hertz-Mindlin model with JKR theory.

Table 9
Comparisons of the contact model for the Elasto-plastic and adhesive contact.

Contact model	Thornton and Ning [10]	Pasha et al. [12]*	Luding [13]	This work
Computational time and complexity	High	Low	Low	Low
Unified mathematical equations	Provided	/	Provided	Provided
Ability to consider both elastic and plastic deformation in dynamic particulate system	Yes	Yes	/	Yes
Rigorous equations to calculate the key parameters	Provided	/	/	Provided
Method to calculate critical sticking velocity considering both elastic and plastic deformation	Part-provided**	/	/	Provided

* It is referred to the full model instead of the simplified version in Pasha et al. [12].
** Effect of elastic and plastic deformation on critical sticking velocity is discussed separately in Thornton and Ning [10].

Table 10
Total computational time used in the simulation cases (Γ = 3.5 mJ/m^2, 73,577 particles) in Section 5.

Cases	Computational time (min)
Hertz model with JKR theory*	514
Contact model proposed in this work (without plastic deformation**)	487
Contact model proposed in this work (with plastic deformation)	512

* Built-in JKRV2 model in EDEM software is used.
** In this case, the yield contact pressure is artificially set to a very high value to ensure the contact is always below the yield point to avoid any plastic deformation.

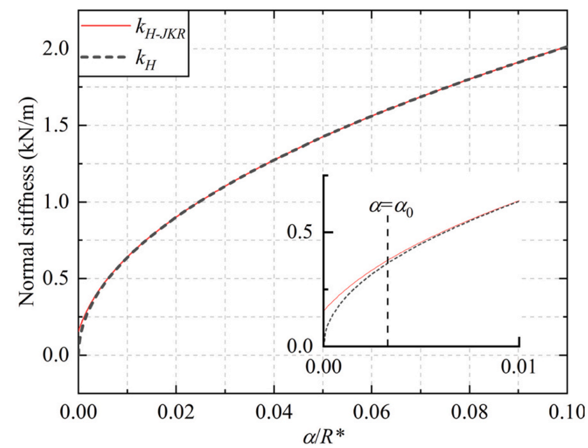

Fig. 13. Variation of normal stiffness with normal overlap in Hertz model and Hertz-JKR model for the case with R^*=2.45 μm, E^*=1.3 GPa and Γ=0.2 J/m^2.

$$\mathrm{CY} = \frac{{p_y}^3 R}{E^2 \Gamma} \tag{81}$$

$CY < 1$ indicates the occurrence of adhesion-induced plastic deformation. It is also close to the ratio of f_{y0}/f_{ce}, which is 1.1 times of CY. For a given material, with a decrease in particle size, CY decreases, and there is a critical particle size, beyond which adhesion-induced plastic deformation could occur (i.e. the attractive force itself could induce plastic deformation). Below this critical particle size, the smaller the particle size, the more cohesive the particle behaves than the one predicted by traditional JKR theory. Namely, particle needs to be more cohesive (i.e. larger surface energy) in JKR theory to get the same critical sticking velocity as predicted by the ones with plastic deformation.

The plastic adhesive sticking velocity V_{ys} is also examined by comparing the value predicted by the contact model in this work with the experimental data of Wall et al. [27], as shown in Fig. 10 and Table 6. Four particle radius are used, i.e. R = 3.445, 2.45, 1.72 and 1.29 μm, with other physical properties shown in Table 5. For the cases without considering viscous damping (i.e. e_0 = 1), V_{ys} is analytically calculated by solving Eqs. (78, 79). For the cases considering viscous damping, a DEM simulation is carried out, and the corresponding restitution coefficient in Eq. (26) is set to be e_0 = 0.81, which corresponds to the limit restitution coefficient in Wall [27]. Viscous damping leads to larger value of V_{ys}, with a relative increment of about 10%, as shown in Table 6. It is clear that considering both viscous damping and plastic deformation in the simulation could lead to a better agreement with the experimental data of Wall et al. [27]. As shown in Table 6, the critical sticking velocity V_{ys} is much larger than the one V_s predicted by JKR theory, and the difference increases with the decrease in particle size.

5. Flowability of bulk powder

To investigate the combined effects of cohesion and plastic deformation on the flowability of bulk powder, the particulate system of FT4 rheometer is simulated, where a twisted blade rotates anti-clockwise while penetrating down into a particle bed, as shown in Fig. 11. The input mechanical work expended for the blade motion is recorded and referred as the flow energy, which can be used to infer the flowability of the powder, i.e. powder with poor flowability (e.g. very cohesive) usually corresponds to large flow energy. More details can be found in the work of Pasha et al. [3] and Nan et al. [28]. As detailed information for both the parameters of single particle and corresponding bulk test is also not available together in the literature, only DEM simulation is carried out in this section.

In the DEM simulations, the diameter of the blade and vessel (cylinder) is 23.5 mm and 25 mm, respectively. The particle radius is 0.4–0.6 mm, with an averaged value of 0.5 mm. The total particle number is 73,577, forming an initial particle bed height of 19 mm. To reduce the computational time, the tip speed of the blade is set to 0.25 m/s, and only the first 10 mm penetration depth is simulated. The physical properties of particle and geometry walls are shown in Table 7, and the corresponding interaction parameters are shown in Table 8. Two surface energies are used for particle-particle interaction, i.e. 3.5 and 27 mJ/m^2, while the surface energy for particle-wall interaction is constant in all cases. Thus, when considering plastic deformation, based on $p_y = 0.5$ MPa shown in Table 7, the cohesion-yield number (Eq. (81)) for particle-particle interaction ($R^* = R/2$) is $CY = 4.2$ for $\Gamma = 3.5$ mJ/m^2, and $CY = 0.5$ for $\Gamma = 27$ mJ/m^2, respectively.

By using the linear elasto-plastic and adhesive contact model developed in this work, two systems are simulated here: with and without considering plastic deformation. In the former, plastic stiffness k_p is assumed to be equal to k_{el}, and k_{el} is given by Eq. (52) with the yield contact pressure of particles shown in Table 7. In the latter, stiffness k_{el} has the same value as that of the former, while the yield contact pressure is artificially set to a very high value to ensure the contact is always below the yield point to avoid any plastic deformation. The corresponding DEM simulation using Hertz model with JKR theory is also conducted as a reference case.

Fig. 12 shows the flow energy of cohesive powder in FT4 rheometer, where the flow energy is calculated at the penetration depth of 10 mm and normalised by the value predicted by the DEM simulation using Hertz-Mindlin model with JKR theory. For the case without considering plastic deformation, the flow energy predicted by the contact model in this work is very close to the ones predicted by the simulations using Hertz-Mindlin model with JKR theory for the two surface energies used. It is obvious that the powder behaves more "cohesively" when considering plastic deformation, especially for the case with larger surface energy. These findings also agree well with the snapshots in Fig. 11.

6. Discussions

For the elasto-plastic and adhesive contact, only a limited number of models are available to estimate the contact force of particles for DEM simulations, i.e. the non-linear model of Thornton and Ning [10], the linear models of Pasha et al. [12] and Luding [13]. Compared to these models, the newly developed model in this work shows huge improvements in terms of physical nature and computational time, which are described in detail below and summarised in Table 9.

The proposed model in this work is a linear version of the non-linear model of Thornton and Ning [10], but its physical nature is well kept. Compared to Thornton and Ning's model, the proposed contact model has several advantages: 1) much less computational time. The governing equations of the non-linear model of Thornton and Ning [10] are in a very complex form. As their model is not available in commercial and open-source DEM software packages, the detail of the computational time is not available. However, it is expected that Thornton and Ning's model will be very computationally expensive for DEM simulation of industrial particulate systems due to its non-linearity nature. For the particulate system in Section 5, the total computational time of the newly developed model is on par with Hertz model with JKR theory, as shown in Table 10, where 10 CPU cores on DELL PowerEdge T640 workstation are involved. 2) more straight-forward. The critical sticking velocity and restitution coefficient can be easily derived to consider the effect of cohesion and plastic deformation concurrently, while these two effects are derived separately in Thornton and Ning [10] due to the complexity of the governing equations.

The proposed contact model has several additional advantages: 1) Compared to Pasha et al. [12], thorough unified mathematical equations are formally presented here, as shown in Section 2, making it easy for implementation in DEM software packages with low computational time, while no similar mathematical framework could be accessed in Pasha et al. [12]. 2) Compared to Luding [13], both the initial elastic and plastic deformation could be considered here, making it more realistic, i.e. in dynamic particulate systems, the external load applied on the particles at some regions is not large enough to cause yielding, and hence the contact is still elasto-adhesive. 3) Compared to both linear models of Pasha et al. [12] and Luding [13], rigorous equations are proposed here to calculate the key parameters (such as stiffnesses and maximum pull-off force). On the contrast, the models Pasha et al. [12] and Luding [13] involves a number of key parameters which is not accessible from single particle characterisation. The proposed contact model is also well validated against the numerical simulation (FEM) and experimental work in literature. 4) Compared to both linear models, the physical nature of contact is well kept during the derivation, for example, both the adhesive sticking velocity predicted by JKR theory and plastic work predicted by plasticity theory are guaranteed in the proposed contact model. 5) Compared to both linear models, the number of parameters required for experimental characterisation in the proposed contact model is minimised, for example, compared to Hertz model with JKR theory, only the yield stress is additionally required in some cases, which is also summarised in Section 3.6.

The proposed contact model could be reduced to simpler case, such as elasto-adhesive contact, elasto-plastic contact, as shown in Sections 2 & 3. It is therefore applicable for DEM simulation of most particulate systems. Of course, the focus of the proposed contact model is mainly on elasto-plastic and adhesive contact. For particles with $CY < 1$, the effect of plastic deformation on the behaviour of cohesive powder must be taken into account. Plastic deformation could also have a significant effect on bulk behaviour of cohesive powder if the characteristic velocity of the particulate system is larger than the yield velocity V_y.

7. Conclusions

Based on the work of Thornton and Ning [10] and Pasha et al. [12], an improved linear model is developed for elasto-plastic and adhesive contact in DEM simulation. This contact model is then applied to the analysis of single particle impact test and the DEM simulation of bulk particle behaviour in FT4 rheometer. The main results from the present study are summarised as follows:

1) A general and mathematic form is proposed for the contact model, with new correlations to estimate the parameters involved in the model, including various stiffnesses (k_e, k_p, k_c), yield point, maximum pull-off force and time step. The physical nature of contact is well kept during the derivation, and the correlations are validated against the data extracted from the literature. Compared to previous contact models, the number of parameters required for experimental characterisation is minimised in the proposed contact model.
2) The adhesive work and yield work are guaranteed to be the same as the non-linear model of Thornton and Ning [10]. The stiffness in the unloading process is scaled to the square root of the maximum overlap at which unloading commences. The maximum pull-off force increases with the plastic deformation, and it can be reduced to the form predicted by JKR theory if the contact is not yielded. The estimation correlations for elastic stiffness and maximum pull-off force are validated by the loading/unloading curves reported in the literature. The time step can be evaluated based on Rayleigh time step.
3) A new correlation is proposed to calculate the plastic adhesive sticking velocity. The sticking velocity of cohesive particle with a small yield contact pressure is larger than the one predicted by JKR theory. The contact model developed in this work is also validated by comparing the sticking velocity predicted against the experimental data in literature.
4) A cohesion-yield number is proposed to describe the extent of adhesion-induced yielding, in which the attractive force would always induce plastic deformation as long as the particles can be

brought into contact. For the particle below critical size, the effect of plastic deformation should be considered and the particles behaves more "cohesively" than the ones predicted by JKR theory.

5) The flowability of bulk powder is strongly affected by the plastic deformation, especially for the particles with large surface energy. The bulk powder in FT4 rheometer behaves more "cohesively" if considering plastic deformation.

CRediT authorship contribution statement

Wenguang Nan: Conceptualization, Investigation, Formal analysis, Writing – original draft, Writing – review & editing. **Wei Pin Goh:** Writing – review & editing. **Mohammad Tarequr Rahman:** Writing – review & editing.

Declaration of Competing Interest

The authors declare that they have no known competing financial interests or personal relationships that could have appeared to influence the work reported in this paper.

Acknowledgments

The first author is grateful to the National Natural Science Foundation of China (Grant No. 51806099). The authors are also thankful to DEM Solutions, Edinburgh, UK, for providing a special license for the EDEM software for use in this work. The first author is also thankful to Professor Mojtaba Ghadiri, University of Leeds, UK, for the inspiration and encouragement on this work.

Appendix A

The work of deformation due to normal contact force in each stage in Fig. 4 is derived as follows:

$$W_0 = \frac{1}{2}\left(\alpha_{ce} - \alpha_{fe}\right)\left(\frac{5}{9}f_{ce} + f_{ce}\right) + \frac{1}{2}\alpha_{ce}\left(\frac{8}{9}f_{ce} + f_{ce}\right) = \frac{56}{162}\frac{f_{ce}{}^2}{k_{cl}} + \frac{17}{162}\frac{f_{ce}{}^2}{k_{el}} \tag{A1}$$

$$W_1 = \frac{f_0{}^2}{2k_{el}} = \frac{64}{162}\frac{f_{ce}{}^2}{k_{el}} \tag{A2}$$

$$W_2 = \frac{f_y{}^2}{2k_{el}} \tag{A3}$$

$$W_3 = \frac{1}{2}\left(f_y + f_{\max}\right)\cdot\left(\alpha_{\max} - \alpha_y\right) - \frac{1}{2}f_{\max}\left(\alpha_{\max} - \alpha_p\right) = \frac{\left(f_{\max}{}^2 - f_y{}^2\right)}{2k_p} - \frac{f_{\max}{}^2}{2k_e} \tag{A4}$$

$$W_4 = \frac{f_{\max}{}^2}{2k_e} \tag{A5}$$

$$W_5 = \frac{1}{2}\frac{\left(\frac{8}{9}f_{cp}\right)^2}{k_e} = \frac{64}{162}\frac{f_{cp}{}^2}{k_e} \tag{A6}$$

$$W_6 = \frac{1}{2}\left(\alpha_{cp} - \alpha_{fp}\right)\left(\frac{5}{9}f_{cp} + f_{cp}\right) + \frac{1}{2}\left(\alpha_{c0} - \alpha_{cp}\right)\left(\frac{8}{9}f_{cp} + f_{cp}\right) = \frac{56}{162}\frac{f_{cp}{}^2}{k_c} + \frac{17}{162}\frac{f_{cp}{}^2}{k_e} \tag{A7}$$

Appendix B

In the Hertz model with JKR theory, the contact force and normal stiffness are given as:

$$f_{H-JKR} = \frac{4E^* a^3}{3R^*} - \sqrt{8\pi\Gamma E^*}\,a^{3/2} \tag{B1}$$

$$k_{H-JKR} = 2E^* a\frac{\sqrt{f_H/f_{ce}} - 1}{\sqrt{f_H/f_{ce}} - 1/3} \tag{B2}$$

where $f_{ce} = 1.5\pi\Gamma R^*$; a is the contact radius; f_H is the equivalent Hertz force with the same contact radius. a and f_H are given as:

$$\alpha = \frac{a^2}{R^*} - \left(\frac{2\pi\Gamma a}{E^*}\right)^{1/2} \tag{B3}$$

$$f_H = \frac{4E^* a^3}{3R^*} \tag{B4}$$

where α is the normal physical overlap. At the point $\alpha = 0$, the contact radius is given as:

$$a = \left(2\pi\frac{\Gamma R^{*2}}{E^*}\right)^{1/3} \tag{B5}$$

Substituting Eq. (B5) into Eqs. (B4) and (B2), given as:

$$f_H \Big/ f_{ce} = \frac{16}{9} \tag{B6}$$

$$k_{H-JKR,\alpha=0} = \left(\frac{16}{27}\pi\right)^{1/3} \left(\Gamma E^{*2} R^{*2}\right)^{1/3} \tag{B7}$$

Similarly, at the point $\alpha = \alpha_0$, the contact force $f_{H\text{-}JKR} = 0$, given as:

$$a = \left(\frac{9\pi}{2} \frac{\Gamma R^{*2}}{E^*}\right)^{1/3} \tag{B8}$$

$$f_H / f_{ce} = 4 \tag{B9}$$

$$k_{H-JKR,\ \alpha=\alpha_0} = \frac{6}{5}\left(\frac{9}{2}\right)^{1/3} \pi^{1/3} \left(\Gamma E^{*2} R^{*2}\right)^{1/3} \tag{B10}$$

$$\alpha_0 = \left(\frac{3}{4}\right)^{1/3} \left(\frac{\pi^2 R^* \Gamma^2}{E^{*2}}\right)^{1/3} \tag{B11}$$

At this point, the normal stiffness of Hertz model with the same overlap is given as:

$$k_{H,\ \alpha=\alpha_0} = 2E^* \sqrt{R^* \alpha_0} = 2\left(\frac{3}{4}\right)^{1/6} \pi^{1/3} \left(\Gamma E^{*2} R^{*2}\right)^{1/3} \tag{B12}$$

By comparing (B12) and (B10), given as:

$$\frac{k_{H-JKR,\ \alpha=\alpha_0}}{k_{H,\ \alpha=\alpha_0}} = \frac{3\sqrt{3}}{5} \approx 1.04 \tag{B13}$$

Thus, for the normal overlap larger than α_0, i.e. $f_{H\text{-}JKR} > 0$, the normal stiffness in Hertz model with JKR theory (Eq. (B2)), could be estimated by the ones predicted by Hertz model (Eq. (41)) at the same normal overlap, which is also clear illustrated in Fig. 13.

Appendix C. Supplementary data

Excel worksheet is provided for quick calculation of the parameters involved in the proposed contact model and the critical sticking velocity. Supplementary data to this article can be found online at https://doi.org/10.1016/j.powtec.2022.117634.

References

[1] P.A. Cundall, O.D.L. Strack, A discrete numerical model for granular assemblies, Géotechnique 29 (1979) 47–65.
[2] W. Nan, M. Pasha, T. Bonakdar, A. Lopez, U. Zafar, S. Nadimi, M. Ghadiri, Jamming during particle spreading in additive manufacturing, Powder Technol. 338 (2018) 253–262.
[3] M. Pasha, N.L. Hekiem, X. Jia, M. Ghadiri, Prediction of flowability of cohesive powder mixtures at high strain rate conditions by discrete element method, Powder Technol. 372 (2020) 59–67.
[4] M.W. Johnstone, Calibration of DEM Models for Granular Materials Using Bulk Physical Tests, University of Edinburgh, 2010.
[5] C. Thornton, Granular Dynamics, Contact Mechanics and Particle System Simulations, Springer, New York, 2015.
[6] K. Johnson, K. Kendall, A. Roberts, Surface energy and the contact of elastic solids, Proceedings of the Royal Society of London. A. Mathematical and Physical Sciences 324 (1971) 301–313.
[7] B.V. Derjaguin, V.M. Muller, Y.P. Toporov, Effect of contact deformations on the adhesion of particles, J. Colloid Interface Sci. 53 (1975) 314–326.
[8] M. Pasha, C. Hare, M. Ghadiri, A. Gunadi, P.M. Piccione, Effect of particle shape on flow in discrete element method simulation of a rotary batch seed coater, Powder Technol. 296 (2016) 29–36.
[9] W.G. Nan, M. Pasha, M. Ghadiri, Effect of gas-particle interaction on roller spreading process in additive manufacturing, Powder Technol. 372 (2020) 466–476.
[10] C. Thornton, Z. Ning, A theoretical model for the stick/bounce behaviour of adhesive, elastic-plastic spheres, Powder Technol. 99 (1998) 154–162.
[11] O.R. Walton, R.L. Braun, Viscosity, granular-temperature, and stress calculations for shearing assemblies of inelastic, frictional disks, J. Rheol. 30 (1986) 949.
[12] M. Pasha, S. Dogbe, C. Hare, A. Hassanpour, M. Ghadiri, A linear model of elasto-plastic and adhesive contact deformation, Granul. Matter 16 (2014) 151–162.
[13] S. Luding, Cohesive, frictional powders: contact models for tension, Granul. Matter 10 (2008) 235–246.
[14] Z. Ning, Elasto-Plastic Impact of Fine Particles and Fragmentation of Small Agglomerates, Aston University, 1995.
[15] R.L. Jackson, I. Green, A finite element study of Elasto-plastic hemispherical contact against a rigid flat, J. Tribol. 127 (2005) 343–354.
[16] W.R. Chang, I. Etsion, D.B. Bogy, An elastic-plastic model for the contact of rough surfaces, J. Tribol. 109 (1987) 257–263.
[17] H.A. Burgoyne, C. Daraio, Strain-rate-dependent model for the dynamic compression of elastoplastic spheres, Physical Review E 89 (2014), 032203.
[18] C. Thornton, S.J. Cummins, P.W. Cleary, On elastic-plastic normal contact force models, with and without adhesion, Powder Technol. 315 (2017) 339–346.
[19] Y. Du, L. Chen, N.E. McGruer, G.G. Adams, I. Etsion, A finite element model of loading and unloading of an asperity contact with adhesion and plasticity, J. Colloid Interface Sci. 312 (2007) 522–528.
[20] A.O. Raji, Discrete Element Modelling of the Deformation of Bulk Agricultural Particulates, Newcastle University upon Tyne, UK, 1999.
[21] U. Zafar, C. Hare, A. Hassanpour, M. Ghadiri, Drop test: a new method to measure the particle adhesion force, Powder Technol. 264 (2014) 236–241.
[22] T.T. Nguyen, C. Rambanapasi, A.H. de Boer, H.W. Frijlink, P.M. Ven, J. de Vries, H. J. Busscher, K. Maarschalk, A centrifuge method to measure particle cohesion forces to substrate surfaces: the use of a force distribution concept for data interpretation, Int. J. Pharm. 393 (2010) 88–95.
[23] J.S. Marshall, S. Li, Adhesive Particle Flow-a Discrete-Element Approach, Cambridge University Press, 2014.
[24] S.D. Mesarovic, K.L. Johnson, Adhesive contact of elastic–plastic spheres, Journal of the Mechanics and Physics of Solids 48 (2000) 2009–2033.
[25] I. Etsion, Y. Kligerman, Y. Kadin, Unloading of an elastic–plastic loaded spherical contact, International Journal of Solids and Structures 42 (2005) 3716–3729.
[26] O.V. Kim, P.F. Dunn, A microsphere-surface impact model for implementation in computational fluid dynamics, J. Aerosol Sci. 38 (2007) 532–549.
[27] S. Wall, W. John, H.-C. Wang, S.L. Goren, Measurements of kinetic energy loss for particles impacting surfaces, Aerosol Sci. Technol. 12 (1990) 926–946.
[28] W.G. Nan, M. Ghadiri, Y.S. Wang, Analysis of powder rheometry of FT4: effect of air flow, Chem. Eng. Sci. 162 (2017) 141–151.